Check for updates

ADVANCED ENERGY MATERIALS
www.advenergymat.de

Mapping the Binary Covalent Alloy Space to Pursue Superior Nitrogen Reduction Reaction Catalysts

Cooper R. Tezak, Sophie Gerits, Benjamin Rich, Christopher Sutton, Nicholas Singstock, and Charles B. Musgrave**

The electrochemical nitrogen reduction reaction (NRR) has the potential to decarbonize industrial ammonia production. However, NRR has poor activity and selectivity versus the competing hydrogen evolution reaction for catalysts that adhere to scaling relations. Overcoming the limitations imposed by scaling relations requires more complex catalyst materials, however, evaluating materials beyond simple metal systems is a large combinatorial problem that requires an improved understanding of the electrocatalyst surface to rationally guide the discovery of superior catalysts. The study uses grand canonical density functional theory to uncover NRR trends on a large and disparate set of binary covalent alloys (BCA) with variable compositions and active-site geometries. The studied BCAs generally follow scaling relations, albeit with larger variance and several systems that significantly break scaling. BCAs with early- to mid-transition metals tend to lie near the volcano peak and activate the N_2 triple bond via a side-on binding configuration. Trends in the BCA space cannot be readily predicted using simple electronic descriptors, which is ascribed to the large geometric variability of the BCA surfaces. It is anticipated that these findings will provide a foundation for the rational design of superior NRR electrocatalysts with increasing material complexity.

1. Introduction

Industrial ammonia synthesis via the Haber Bosch process provides the ammonia feedstock for fertilizers that support nearly half of the world's population, however, it also generates ~2% of global carbon emissions.[1,2] Multiple alternatives have been proposed to lower the carbon intensity of ammonia production. The "green" Haber–Bosch process has been proposed as an alternative low-emissions ammonia synthesis method, but depends on the development of efficient processes to renewably generate hydrogen, for example by hydrogen electrolysis[3] or solar thermal water splitting[4] and still requires large, centralized plants with high capital costs that operate at high temperature and pressure.[5] The electrochemical nitrogen reduction reaction (NRR) is another proposed carbon-free approach for ammonia synthesis that has the advantage of facilitating distributed fertilizer production using renewable electricity, air, and water as precursors.[6,7] However, of the key electrochemical conversion reactions with the potential to enable decarbonization of the chemical and energy sectors, NRR may be the most limited by poor activity and selectivity.[6]

To understand what causes the activity and selectivity challenges of NRR, we used grand-canonical density functional theory (GC-DFT)[8] to study the nitrogen reduction reaction on monometallic catalysts,[9] which universally obey scaling relations.[10,11] These scaling relations are well known by the catalysis community to stem from the linear correlations between adsorbed intermediate binding strengths, which give rise to "volcano plots" that quantify the Sabatier principle.[11] Using bias-dependent GC-DFT calculations that enable the inclusion of both chemical and electrochemical steps in the reaction

C. R. Tezak, S. Gerits, N. Singstock, C. B. Musgrave
Department of Chemical and Biological Engineering
University of Colorado Boulder
Boulder, CO 80309, USA
E-mail: nicholas.singstock@colorado.edu;
charles.musgrave@colorado.edu

B. Rich
Department of Chemistry
University of Colorado Boulder
Boulder, CO 80309, USA

C. Sutton
Department of Chemistry and Biochemistry
University of South Carolina
Columbia, SC USA

N. Singstock
Department of Mechanical Engineering
University of Colorado Boulder
Boulder, CO 80309, USA

C. B. Musgrave
Materials Science and Engineering Program
University of Colorado Boulder
Boulder, CO 80309, USA

C. B. Musgrave
Renewable and Sustainable Energy Institute
University of Colorado Boulder
Boulder, CO 80309, USA

The ORCID identification number(s) for the author(s) of this article can be found under https://doi.org/10.1002/aenm.202304559

DOI: 10.1002/aenm.202304559

 © 2024 Wiley-VCH GmbH

16146840, 0, Downloaded from https://onlinelibrary.wiley.com/doi/10.1002/aenm.202304559 by Office Of Scientific And Technical Information, Wiley Online Library on [28/05/2024]. See the Terms and Conditions (https://onlinelibrary.wiley.com/terms-and-conditions) on Wiley Online Library for rules of use; OA articles are governed by the applicable Creative Commons License

mechanism, we computed revised NRR scaling relations that result in a volcano plot with a truncated peak.[9] The challenge to achieving efficient NRR on metals is that even optimal NRR catalysts that lie at the volcano peak have higher HER activity than NRR activity, such that no metals have yet been identified that are active and selective toward NRR. Moreover, addressing this challenge cannot be achieved simply by applying a more reducing bias to accelerate NRR because HER activity increases with applied potential more than NRR activity.[9] These finding from our previous work, and the general lack of commercially-viable experimental NRR results,[12] highlight that developing effective NRR electrocatalysts is a materials-limited challenge.

To tackle the challenge of identifying catalysts that are both selective and active toward NRR, more complex materials must be explored that can decouple adsorbate binding strengths to break scaling relations. Several published reviews have suggested strategies to break scaling relations, which generally involve increasing the geometric and electronic complexity of catalyst surfaces.[12–14] In particular, a perspective by Pérez–Ramírez and López proposed a framework that categorizes catalyst materials into levels based on increasing geometric and electronic complexity.[13] In their hierarchy, monometallic metals and their simple alloys comprise the first level, *p*-doped metals, and other doped systems comprise the second level, ligand modified and organometallic systems comprise the third level, and externally modulated materials are at the fourth and highest level. While ascending the levels of this materials framework provides opportunities to improve catalyst activity and selectivity, it also combinatorially expands the candidate material space in a field where the evaluation of electrocatalysts demands considerable time and resources.[13] This is especially true for exploratory experimental approaches, but also poses a major challenge to computationally guided catalyst discovery. For this reason, both experimental and computational efforts to evaluate catalyst materials for NRR and for electrocatalysis in general have historically focused on simple metals and alloys that lie within the first tier of the materials complexity framework.

To the best of our knowledge, all efforts to consider materials lying in higher tiers of complexity (≥ 2) have been limited to evaluating single phases or compositional spaces where the catalyst structures are fixed or constrained. Consequently, no published electrocatalysis research effort has yet explored a broad set of materials with highly variable electronic and geometric surface properties. Yet, an effort of this nature is urgently needed to discover NRR catalysts that break traditional metal scaling. A systematic exploration of increasingly complicated materials spaces will facilitate a strategic ascent of the materials complexity framework. In this work, we study a broad set of NRR catalysts that lie within the second level of the material complexity framework by providing a map of the *p*-doped binary covalent alloys (BCAs). By evaluating this second level, fundamental principles governing NRR are extracted, which may be leveraged to guide the rational design of increasingly complex, and better-performing NRR candidates. This study describes the interplay between electronic and geometric effects that emerge at this level to guide the field toward exploring increasingly complex materials. Many of the BCAs considered here are predicted to break linear scaling relations either favorably or unfavorably. The locations of these BCAs on the *x*-axis of the volcano trend with metal group/column, with binaries that contain early- to mid-transition metals (TM) generally being aggregated near the peak of the NRR volcano. Our results predict that some of these materials provide comparable, or even superior activity and selectivity to Ru, which is the current standard NRR reference due to its position near the volcano peak. We rationalize observed trends from both a geometric and an electronic perspective. These results highlight the challenges that arise when attempting to predict binary metal activity using simple bulk catalytic descriptors, such as the *d*-band center, that exclude geometric effects. Building upon our current study and our previous work on NRR electrocatalysts, this paper concludes by offering a perspective on the challenges, opportunities, and strategies within the NRR field. Our aim is to guide the rational ascent of the levels of materials complexity to aid the discovery of materials that strategically break NRR scaling relations at favorable locations on the volcano. Through this approach, we anticipate transformational improvements in NRR activity and selectivity necessary for economically viable electrochemical ammonia synthesis and the opportunity to mitigate ~2% of global carbon emissions.

2. Screening Workflow

We model, evaluate, and compare a relatively large and disparate set of BCA materials with the formula M_xL_y, where M is a cationic metal (e.g., TM, alkali earth, post-TM), and L an anionic nonmetal or metalloid (see **Figure 1**). We limited the BCAs considered to those with stoichiometric ratios x:y between 1:6 and 6:1. This set includes 101 surfaces derived from 86 bulk phases comprising 30 metals and 13 nonmetals, with 84 unique stoichiometries. The resulting surfaces exhibit a wide range of electronic and geometric properties. The large number of surfaces considered demanded the development of a transferable and predominantly automated screening approach that converts the bulk crystal structures into stable surface facets and then screens these candidates as potential NRR catalysts by computing adsorption energies of relevant intermediates at realistic applied potentials using GC-DFT.

We used GC-DFT to model the cathode surface at a fixed applied potential in contact with aqueous electrolyte. GC-DFT self-consistently solves the Kohn-Sham DFT equations with a variable number of electrons consistent with the applied potential.[15] The effects of solvation were modeled using the CANDLE implicit solvation model.[15] GC-DFT computes grand free energies, represented in this work as Φ, that are used to evaluate NRR intermediate adsorption energies and catalytic activity. The scaling of NRR intermediate adsorption grand free energies (Φ_{ads}) and catalytic activity were investigated using the thermodynamic approximation to the energetic span,[16,17] Φ_{max}. This model approximates the activity of a catalytic cycle using the grand free energy difference between the highest and lowest energy intermediates in the pathway. A more thorough discussion of the energetic span and Φ_{max} is provided in Section S1 (Supporting Information), and in our previous work that used this approach with GC-DFT-computed grand free energies to show that pure metals adhere to a revised set of scaling relations.[9]

Our workflow is shown in Figure 1, which illustrates each step of the screening workflow. Step numbers are referenced throughout the text and details about individual screening steps and the GC-DFT method are described in Section S1 (Supporting

 © 2024 Wiley-VCH GmbH

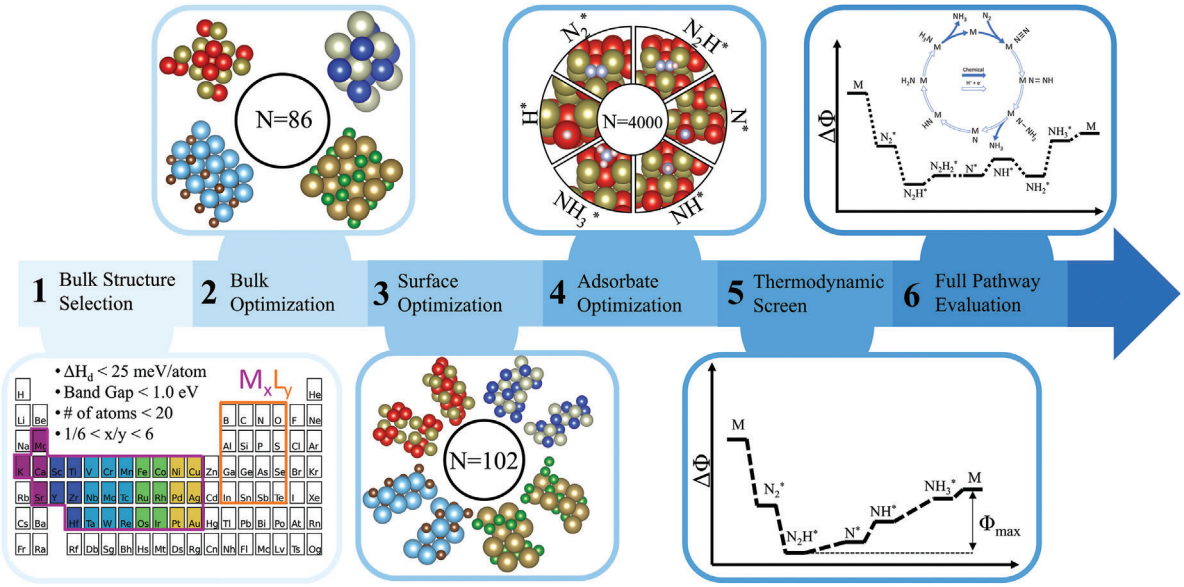

Figure 1. Materials Screening Workflow. **Step 1**: Bulk structures were selected by identifying materials with binary covalent-metal element combinations that exist on Materials Project and meet the criteria shown. **Step 2**: Bulk structures were optimized. **Step 3**: Surface facets were cut using an algorithm that maximizes stability, and then optimized using GC-DFT. **Step 4**: A select subset of NRR adsorbates were placed at active sites on each surface and their adsorption energies were calculated. **Step 5**: Surfaces were evaluated using the Φ_{max} descriptor calculated from the reduced set of adsorbates. **Step 6**: Promising surfaces were further studied by fully sampling adsorbate binding configurations for all states in the associative distal pathway.

Information). In **Step 1**, bulk structures were selected from the Materials Project database[18] based on their stability (i.e., decomposition enthalpy, ΔH_d) and bandgaps with the intention to span a broad range of M-L combinations. A review of the literature was conducted for each bulk material to determine if previous work had demonstrated that the material was synthesizable and stable in aqueous electrolytes (see experimental section for more detail). In **Step 2**, stable surface facets were identified from the optimized bulk structures using a heuristic screening approach developed by Sun and Ceder that identifies facets that minimize the number of broken bonds and maximizes surface atom coordination.[19] These clean surface facets were then optimized in **Step 3** with our automated electrocatalyst screening algorithm, developed for our NRR scaling relations study of metals,[9] using GC-DFT. The scaling relations we previously identified for metals indicated that a reduced set of intermediates limit the activity and selectivity of metal catalysts (i.e., N_2^*, N_2H^*, N^*, NH^*, NH_3^*, H^*); this set was used as a preliminary screening set to evaluate the upper-bound of catalyst activity. We note that our reduced set of intermediates does not include NH_4^+. The results of a set of calculations discussed in section 9 of the SI indicate that NH_4^+ is not a stable adsorbed species, although its formation by protonation of NH_3* may be a kinetically relevant surface-mediated step, especially at low pH. However, if NH_4^+ is in fact formed, then we expect its barrier to formation to correlate well with the adsorption energy of NH_3 and that including this step will not alter the conclusions of this study. In **Step 4**, an automated script was used to place and optimize these adsorbates on multiple active sites on each surface facet. In **Step 5**, Φ_{max}, which represents the largest endergonic grand free energy change between any series of steps in the reaction pathway, was used to estimate the activity of each catalyst (see Section S1, Supporting Information). In **Step 5**, Φ_{max} may yield false positives (i.e., materials with high predicted activity). However, it does not produce false negatives, as adding additional intermediates to the NRR pathway can increase Φ_{max} but will not decrease it. Thus, in **Step 6**, promising materials that survive the preliminary Φ_{max} screening analysis were further evaluated by calculating their full NRR pathways to remove false positives. This two-step screening approach enables the efficient removal of materials that are predicted to not be viable NRR electrocatalysts. Our screening workflow does not calculate kinetic barriers due to the instability and computational expense of algorithms used to calculate barriers.[20] This screening approach may therefore incorrectly identify materials as promising catalysts that deviate from Bronsted Evans–Polanyi behavior.[21] To better understand the underlying materials properties that yield favorable activity and/or scaling-relation-breaking behavior, additional electronic structure methods were used to quantify surface-adsorbate interactions for catalyst candidates that were passed to **Step 6**, although this is not a necessary step of the workflow. This approach may be readily applied to study other material systems with increasing complexity and is transferable to other reactions beyond NRR. The codes developed for this work are published online (see experimental section).

3. Results

3.1. Scaling Relation Trends for the Binary Covalent Alloy Materials

Figure 2A shows the volcano diagrams that emerge from the scaling relations between key NRR intermediates on monometallic surfaces (solid volcano lines).[9] The *x*-axis is the nitrogen atom (N^*) binding energy (i.e., Φ_{N*}, where * indicates an adsorbed

© 2024 Wiley-VCH GmbH

16146840, 0, Downloaded from https://onlinelibrary.wiley.com/doi/10.1002/aenm.202304559 by Office Of Scientific And Technical Information, Wiley Online Library on [28/05/2024]. See the Terms and Conditions (https://onlinelibrary.wiley.com/terms-and-conditions) on Wiley Online Library for rules of use; OA articles are governed by the applicable Creative Commons License

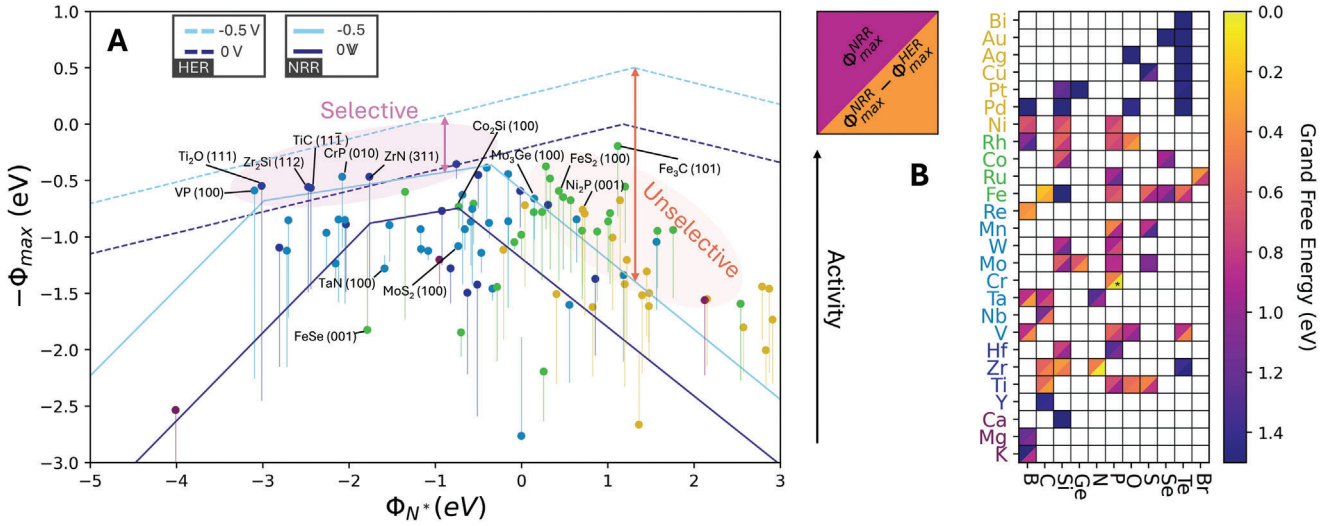

Figure 2. NRR Volcano for Binary Covalent Alloys. A) NRR (solid line) and HER (dashed line) -Φ_{max} volcano plots at 0 V (purple) and −0.5 V (blue) with overlaid BCA results. The colored circles denote -Φ_{max} values of BCAs at −0.5 V and tail ends indicate -Φ_{max} at 0 V. Metal cation identity is denoted by color and corresponds to the coloring scheme of **Step 1** in Figure 1. Many BCAs break scaling above the rightmost scaling line but are unselective. Although no material lies above the HER scaling lines, several materials on the left side of the volcano approach the HER scaling line (higher selectivity). B) Φ_{max} activity (upper left triangles) and selectivity (lower right triangles) for each studied pair of anions/cations. The minimum Φ_{max} surface was used for pairs with multiple stoichiometries and surfaces. Yellow squares are the most active/selective and purple squares are the least active/selective. Ti- and Zr-based BCAs exhibit strong activity/selectivity across anions as do a few Re, Ru, Fe, and Rh BCA surfaces. CrP (*) is starred because it is more selective than the range of the colorbar.

species). -Φ_{max} is plotted on the *y*-axis and serves as a thermodynamic descriptor for electrocatalyst activity that we previously used to define the scaling relations on monometallic surfaces (see Section S1, Supporting Information for details). Note that -Φ_{max} is plotted to obtain the upright volcano orientation, but that lower values of Φ_{max} indicate higher predicted activity. The volcano for HER is also shown (dashed lines) in Figure 2A, where a larger distance between the HER and NRR scaling lines suggests lower NRR selectivity. The highest peak of the volcano is predicted to provide the highest NRR activity; however, the lower left peak of the volcano near −3 eV Φ_{N*} (at −0.5 V) is expected to provide the highest NRR selectivity due to its closer proximity to the HER scaling lines (see Figure S9, Supporting Information). Each scaling line of the volcano represents a step, or series of steps, that dictate Φ_{max}. The line on the volcano's left side constrains the activity of the most reactive metals with stronger N* binding energies (< −1.75 eV at 0 V). The activity of these metals is limited by the double protonation and desorption on NH^* to NH_3 and is highly sensitive to bias due to the transfer of two electrons occurring during these steps. The flatter, central line that truncates the volcano constrains metals with moderate N* binding energies (−1.75 to −0.73 eV at 0 V). Their limiting step is the desorption of $NH_3{}^*$, which is a chemical step and is therefore less sensitive to changes in applied potential. The scaling line on the volcano's right side limits the less reactive metals with weaker N* binding energies (> −0.73 eV at 0 V). These metals are restricted by the desorption of $NH_3{}^*$ and the subsequent adsorption and protonation of N_2 to N_2H^*, which involves one electron transfer.

Φ_{max} was evaluated for all surface facets in the set of BCA materials at 0 and −0.5 V versus the standard hydrogen electrode (SHE). Figure 2A shows the studied BCAs overlaid onto the metal scaling volcanos, colored by cation identity. The studied BCAs are relatively well-dispersed across the scaling volcano, with several materials lying in the promising high activity and selectivity region near the volcano peaks (pink highlighted region). For most BCAs, Φ_{max} decreases under more reducing biases, as expected when electrode-to-molecule electron transfer steps make up Φ_{max}. However, the degree of Φ_{max} bias sensitivity depends on the number of electrons transferred and the electronic structure of the surface, which imparts variability in bias sensitivity across the set of BCA surfaces. Further discussion of bias sensitivity, including surfaces that directionally break the computational hydrogen electrode (CHE)[22] predicted behavior is included in Section S5 (Supporting Information). Compared to flat and stepped monometallic surfaces, the binaries exhibit a greater mean absolute deviation (MAD) from the relevant scaling line at a given Φ_{N*}, with a MAD from scaling of 0.47 eV for binaries versus a MAD of only 0.27 eV for metals. The binaries also have greater variance in their deviation from scaling, with a variance of 0.16 eV compared to 0.03 eV for metals (see Figure S4, Supporting Information). The larger mean and variance in the absolute deviation from scaling suggests that adherence to scaling relations is weakened in the BCA space relative to metal surfaces. The weaker adherence to scaling is attributed to the larger diversity in active site coordination, bulk geometry, and electronic structure relative to monometallic surfaces.

As shown in Figure 2A, the BCAs generally follow the scaling volcano lines of conventional metal surfaces, with most BCAs falling near or below the volcano. This is particularly true near the volcano peak, where materials that adhere to scaling relations are limited by the chemical step of $NH_3{}^*$ desorption. However, it is within this region that we find multiple promising BCA surfaces including TiC (11$\bar{1}$), Zr_2Si (112), CrP (010), and ZrN (311). These materials include early- to mid-TMs paired with less

© 2024 Wiley-VCH GmbH

16146840, 0, Downloaded from https://onlinelibrary.wiley.com/doi/10.1002/aenm.202304559 by Office Of Scientific And Technical Information, Wiley Online Library on [28/05/2024]. See the Terms and Conditions (https://onlinelibrary.wiley.com/terms-and-conditions) on Wiley Online Library for rules of use; OA articles are governed by the applicable Creative Commons License

16146840, 0, Downloaded from https://onlinelibrary.wiley.com/doi/10.1002/aenm.202304559 by Office Of Scientific And Technical Information, Wiley Online Library on [28/05/2024]. See the Terms and Conditions (https://onlinelibrary.wiley.com/terms-and-conditions) on Wiley Online Library for rules of use; OA articles are governed by the applicable Creative Commons License

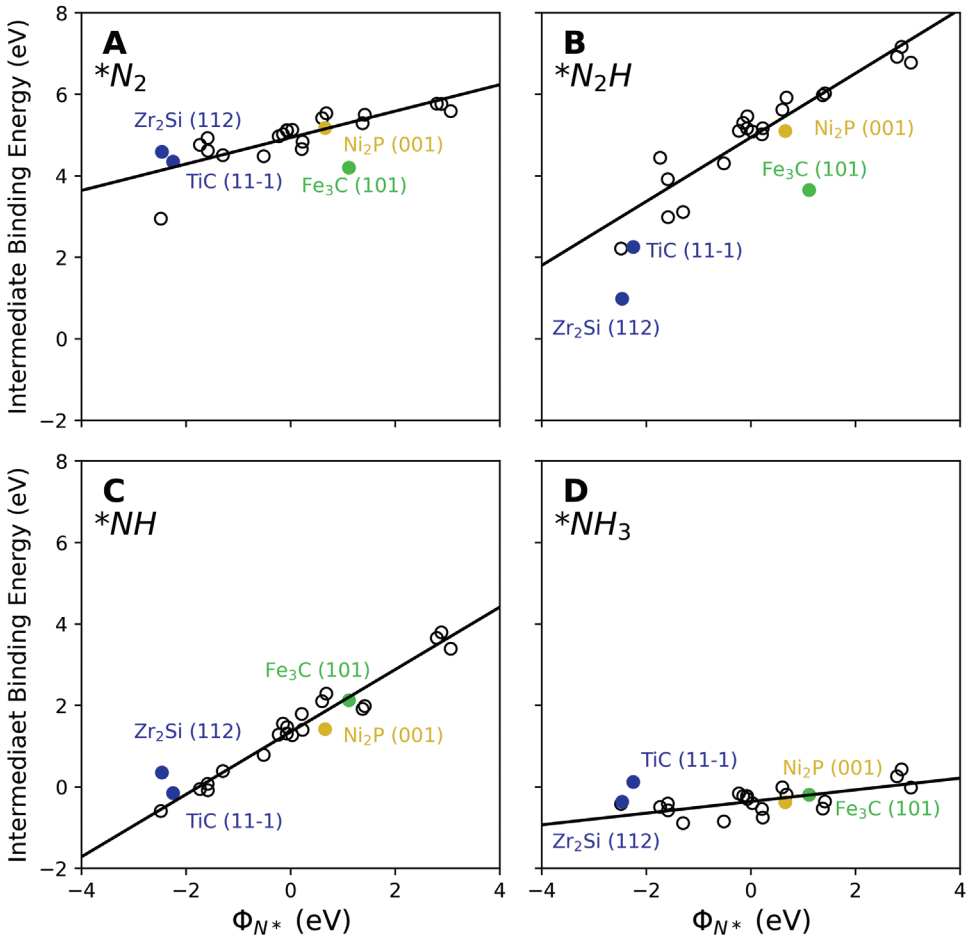

Figure 3. Intermediate Scaling Deviation. Four NRR adsorbate binding energies, A) N_2^*, B) N_2H^*, C) NH^*, and D) NH_3^* from the reduced mechanism intermediate set used in screening **Step 4** were plotted versus the N^* binding energy. Open circles are flat and stepped monometallic surfaces and colored points are binary covalent alloys. All shown binaries selectively stabilize the N_2H^* state relative to metals, with Fe_3C (101) stabilizing it so strongly that the surface reaches the top of the volcano. TiC ($11\bar{1}$) selectively destabilizes NH_3^* and Zr_2Si (112) selectively destabilizes NH^*, both of which promote those surfaces to the top of the volcano.

electronegative anions (e.g., Si, C, P, N). As can be seen in Figure 2B, the early- to mid-TMs tend to yield more active and selective BCAs, especially when coordinated with anions of moderate oxidizing strength. Thus, the promising BCAs for NRR, which have stronger N^* binding and lie near the volcano peak, tend to contain active sites with more reactive metals that have not been highly oxidized by their coordinating anions. Despite this high reactivity, materials such as TiC and ZrN are known to be highly stable in ambient and aqueous conditions,[23–25] which is not the case for monometallic metals in this region of the volcano (e.g., Cr, V, Zr).[26]

Several key observations are identified for the BCA materials that are discussed in detail below: 1) The metal NRR scaling relations act more as an upper bound on BCA predicted activity than a strict criterion that BCAs adhere to, with many BCAs deviating well below the volcano, 2) several BCAs are observed to break scaling relations, both favorably (above the volcano) and unfavorably (below the volcano), 3) favorable breaking of scaling relations tends to occur on the right side of the volcano via stabilization of early intermediates relative to Φ_{N^*}, and 4) N^* binding trends with the periodic table group number (i.e., valence electron count) of the BCA cation, where surfaces lying near the volcano peak are predominantly BCAs containing early- to mid-group TMs (e.g., Ti, Zr). The following sections provide a deeper examination of these materials and observations.

3.2. Chemical Insights from Individual Material Studies

On the reactive side of the volcano (i.e., $\Phi_{N^*} < -1$ eV), there are several catalysts that lie slightly above the volcano or near its peak. NRR intermediate energies were plotted in **Figure 3** for N_2^*, N_2H^*, NH^*, and NH_3^* versus N^* for a select set of BCAs and monometallic surfaces to compare individual intermediate binding energies of BCA surfaces to metal scaling. TiC ($11\bar{1}$) and Zr_2Si (112) possess high predicted activity due to their favorable breaking of N_2^* and N_2H^* scaling (Figure 3A,B). Φ_{max} for TiC ($11\bar{1}$) is limited by NH^*, which scales approximately with metals. Zr_2Si (112) deviates favorably from scaling relations for all the states studied in screening **Step 5**, which initially placed it as

 © 2024 Wiley-VCH GmbH

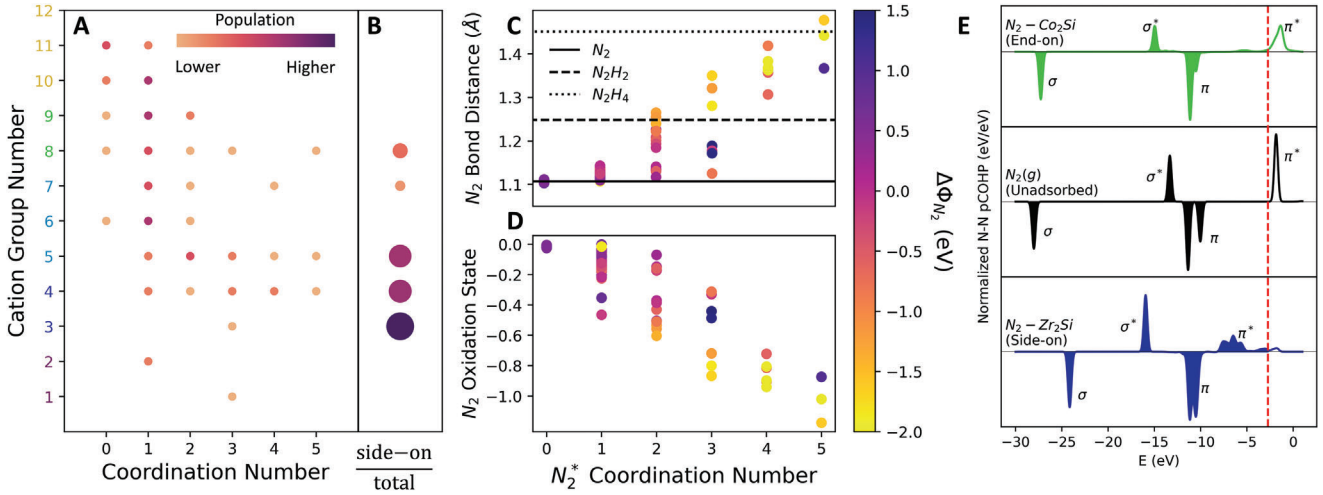

Figure 4. Side binding trends across the binary covalent alloys and their impact on N_2 activation. A) Population of N_2^* coordination number versus material cation group number. Darker shading indicates greater populations. B) Ratio of N_2^* side-on structures to total structures by group number. Early-TM based BCAs prefer side-binding, while later-TMs do not. C) N_2^* coordination versus N_2^* bond length, which shows N_2 bond activation. Horizontal lines for N-N bond length in N_2, N_2H_2, and N_2H_4 are provided as reference triple, double, and single bond lengths. Labels are colored by N_2 binding energy. Greater coordination is correlated to increased N_2 bond activation and binding strength. D) N_2^* Bader charges versus coordination number, indicating greater reduction of N_2 with increased coordination. E) N-N pCOHP distributions for N_2. Negative peaks (up) signify bonding, and positive peaks (down) signify antibonding. The Fermi level is indicated by the red, dashed line. Associated structures are shown in Figure S11 (Supporting Information). pCOHP for side-on binding deviates from free N_2, showing signs of activation, including reduced σ/σ^* splitting, and a downshifted π^* state. End-on σ/σ^* splitting is closer to free N_2, indicating less activation.

the highest activity surface of the BCAs considered. However, after fully evaluating the associative distal pathway (screening **Step 6**), it was found that Zr_2Si (112) over-binds NH_2^*, which becomes the limiting state in the energetic span. This material demonstrates that Φ_{max} acts as an upper limit on catalyst activity when evaluating a reduced set of intermediates, which can decrease as the full reaction pathway is calculated.

Given the positions of TiC ($11\bar{1}$) and Zr_2Si (112) on the volcano, it might initially seem that they are limited by the bias-insensitive desorption of NH_3^*. However, the limiting steps for TiC ($11\bar{1}$) are NH^* to NH_3, and for Zr_2Si (112) are NH_2^* to NH_3. Because these involve formal electron transfers, as a more reducing bias is applied, these two surfaces shift upward more than the minimally bias-sensitive central scaling line of NH_3^* desorption, effectively breaking away from the volcano. At a certain bias, all the electrochemical steps in the reaction mechanism that include an electron transfer will be exergonic, and the only remaining endergonic step will be the chemical step of NH_3^* desorption. Therefore, selectively destabilizing NH_3^* is crucial for achieving further activity promotion. TiC ($11\bar{1}$) successfully breaks NH_3^* scaling relations by selectively destabilizing the bound NH_3^* state by nearly 1 eV (Figure 3D), making it an even more promising surface as its Φ_{max} is strongly dependent on bias. TiC ($11\bar{1}$) is one of the few surfaces in the dataset that does not bind NH_3 in a perfectly on-top position (see SI Figure S11G, Supporting Information), but rather translates the NH_3^* to bind on the side of an undercoordinated Ti atom, suggesting that the d_{z^2} orbital on the Ti atom is unable to participate in favorable bonding with the HOMO on the NH_3 molecule (see Section S8, Supporting Information). TiC ($11\bar{1}$) and its mechanism for selective destabilization of NH_3^* offer an avenue to design reactive catalysts that are highly active at reductive potentials by modulating the occupation of the d_{z^2} orbitals on metal active sites.

Unfortunately, at −0.5 V, Φ_{max} for HER is also small (e.g., 0.22 eV for TiC ($11\bar{1}$), and 0.42 eV for Zr_2Si (112)) and remains bias-sensitive due to the formal electron transfers in both steps of the reaction. Thus, successfully outcompeting HER is still unlikely on these surfaces even at more reducing biases where TiC ($11\bar{1}$) and Zr_2Si (112) break above the NRR volcano further. However, lying near TiC ($11\bar{1}$) and Zr_2Si (112) on the volcano is CrP (010), which we predict also has relatively high NRR activity. Additionally, despite lying below the HER scaling line, CrP (010) has a lower Φ_{max} for NRR than HER, suggesting favorable selectivity toward NRR. This occurs due to the transfer of H^* from Cr sites (at 0 V) to P sites at −0.5 V, where it becomes over-stabilized via reduction by the P atom to yield hydridic H^*, which binds more strongly than would be predicted by the HER scaling line at the corresponding Φ_{N^*}. Thus, CrP (010) is the only surface in the BCA dataset that is precited to have more favorable activity toward NRR than HER, which it achieves by unfavorably breaking HER scaling (i.e., lower HER activity).

For all these surfaces, N_2^* binding is far more favorable than H^* binding, which opens the possibility that higher surface coverages of N_2^* than H^* could be achieved, promoting NRR over HER turnovers. Furthermore, TiC ($11\bar{1}$) and Zr_2Si (112) have sufficiently reactive metal centers to accept donated π electron density from the N_2 molecule to bind N_2^* in a side-on configuration, which we show in **Figure 4** increases the activation of the N_2 triple bond more than the end-on binding configuration and increases N_2^* binding to the surface. This side-on binding configuration also occurs in certain molecular nitrogenase catalysts to activate the otherwise inert N_2.[27]

© 2024 Wiley-VCH GmbH

16146840, 0, Downloaded from https://onlinelibrary.wiley.com/doi/10.1002/aenm.202304559 by Office Of Scientific And Technical Information, Wiley Online Library on [28/05/2024]. See the Terms and Conditions (https://onlinelibrary.wiley.com/terms-and-conditions) on Wiley Online Library for rules of use; OA articles are governed by the applicable Creative Commons License

On the less reactive side of the volcano ($0 < \Phi_{N^*} < 2$ eV) there are many surfaces clustered above the volcano scaling line. Fe_3C (101) and Ni_2P (001) are two representative surfaces of this group that favorably break scaling relations by stabilizing the N_2^* and N_2H^* states relative to N^*, similar to our previous study of a Fe-based multinary catalyst that breaks NRR scaling.[28] Fe_3C (101) shows an especially strong stabilization because it can access the side-on binding motif, which binds N_2^* much more favorably than the end-on motif. Fe_3C (101) has a Φ_{max} comprised of N_2H^* to N^* at 0 V, which switches to the chemical desorption of NH_3^* as the bias becomes more reducing and the N^* state becomes more favorable. Because the NH_3^* state scales approximately with the N^* binding energy on Fe_3C (101) and N^* binding is relatively weak on this surface, the NH_3^* state is also weakly bound, yielding a low Φ_{max} of only 0.19 eV at −0.5 V. Fe_3C (101) exhibits the largest favorable breaking of scaling relations amongst all BCA surfaces studied here, however it is also predicted to have high HER activity, lying in-line with the peak of the HER volcano. Ni_2P (001) deviates less from the volcano scaling lines ($\Phi_{max} = 0.58$ eV at −0.5 V) than Fe_3C (101) because it does not stabilize the N_2H^* state as strongly as Fe_3C (101).

HER activity is predicted to be high for both Ni_2P (001)and Fe_3C (101) because all HER steps are exergonic at −0.5 V ($\Phi_{max} < 0$ eV). H^* binding is more favorable than N_2* binding at 0 V and −0.5 V on Ni_2P (001), which suggests that high surface coverage of NRR intermediates is unlikely and surface sites will instead be predominantly covered by H^*. Fe_3C (101) on the other hand does preferentially bind N_2^* at 0 V, although H^* binding becomes more favorable at −0.5 V. Fe_3C (101) shows a possible path to alloy mid-d block TMs with less oxidizing covalent species to enable the side-on binding mode while preserving the weaker binding of the later NH_x^* states that otherwise limit more reactive surfaces.

3.3. Activation of N_2 Triple Bond Through Side Binding

Figure 4A,B show that across the set of considered BCAs, those with more reactive metal cations (i.e., early *d*-block elements) have a stronger preference to coordinate N_2 with more surface atoms in the side-on configuration, whereas BCAs with less reactive metal cations tend to bind N_2 in the end-on configuration. For metals of Group 9 and greater, no surface was predicted to adsorb N_2 in a side-on binding configuration (coordination number ≥ 3), whereas for Groups 4 and 5, 71% and 60% of the studied surfaces, respectively, bind N_2 side-on. Figure 4C,D show that higher coordination of N_2 to metal surfaces increasingly activates its triple bond, as assessed via lengthening of the N_2 bond and additional charge density localization on the molecule indicated by its Bader charges.[29] The excess electron localization indicates additional electron occupation of the N_2 π^*states, which is confirmed through electronic structure analysis and has been observed previously.[30] Combining the broad trends of metal cation identity and N_2 bond activation produces a clear trend: BCAs with more reactive metals activate the N_2 triple bond better by coordinating more surface atoms to the molecule. Reference N_2, N_2H_2 (diazene), and N_2H_4 (hydrazine) bond lengths show that BCA surfaces can activate the N_2 bond to net bond orders of one, with one surface, TaB (021), even stretching the molecule beyond the bond length of the single N-N bond of hydrazine, which could potentially enable dissociative N_2^* adsorption under mild conditions.

Bond activation was further studied from an electronic perspective using projected Crystal Orbital Hamiltonian Population (pCOHP)[31] analysis on surfaces that progressed to the final screening step (**Step 6** of Figure 1). This analysis utilizes atomic orbital projections and their overlap to the Kohn-Sham wavefunctions to provide a distribution of bonding (negative) and anti-bonding (positive) states. This distribution may also be integrated up to the Fermi level (i.e., ipCOHP) to provide a metric for net bonding. Analysis of the N_2 pCOHP distribution indicates N_2 triple bond activation via reduced splitting of the N_2 σ/σ^* peaks (i.e., the bonding and anti-bonding peaks move closer together) and smearing of the N_2 π^* states, which indicates coupling to less localized, broader surface states. End-on adsorption leaves the bonding/anti-bonding character of N_2 largely unchanged (e.g., Co_2Si (100) in Figure 4E), with minimally reduced splitting and mild π^* broadening. These subtle changes in the electronic character are contrasted by those computed for systems that are predicted to bind N_2 in a side-on binding configuration (e.g., Zr_2Si (112)) in Figure 4E). For the side-on bound systems, σ/σ^* splitting is much smaller than for end-on bound systems, π^* states show broader smearing, and π^* states are relaxed in energy to allow for electron occupation. For some side-bound systems, the π^* state's energy is relaxed to intersect with the Fermi level, which manifests as bias-dependent N_2 adsorption, meaning that the applied electrode potential could be used as an additional lever to tune N_2 binding favorability. For cases where the interaction is so strong that the π^* state stabilizes below the Fermi level, the bias dependence of the N_2 adsorption energy is predicted to disappear and the applied electrode potential cannot be used to tune N_2 binding. The N_2 triple bond activation is also evident in longer N-N bonds (Figure 4C) and reduced N-N ipCOHPs (Figure S2, Supporting Information). Thus, the side-on bonding that is frequently observed for the early- to mid-TM based BCAs facilitates activation and elongation of the N_2 triple bond to promote N_2 binding and the early NRR steps. This side-on binding relies on both suitable active site electronic and geometric structure. The discussion presented here is further supported using a data mining technique known as subgroup discovery. This technique identifies two subgroups (SGs) that exhibit the largest positive and negative binding energies, based on electronic and geometric structural features (see Section S6 and Figure S17, Supporting Information). Specifically, these SGs have ϕ_{N^*} values shifted positively and negatively by factors of 10 and 13, respectively, covering only 25% and 15% of the population. The key features influencing the selection of these SGs are the bond between the N atoms and the binding energy of the N_2^* intermediates, as well as the number of *d* electrons on the metal active sites.

3.4. Electronic Descriptors

To understand what chemical properties are responsible for the observed activity, catalysis researchers often turn to electronic structure properties to describe surface-adsorbate bonding interactions.[32,33] The center of the *d*-band is a widely used descriptor for explaining and predicting activity of simple metals. The *d*-band centers scale strongly with N^* adsorption free

© 2024 Wiley-VCH GmbH

16146840, 0, Downloaded from https://onlinelibrary.wiley.com/doi/10.1002/aenm.202304559 by Office Of Scientific And Technical Information, Wiley Online Library on [28/05/2024]. See the Terms and Conditions (https://onlinelibrary.wiley.com/terms-and-conditions) on Wiley Online Library for rules of use; OA articles are governed by the applicable Creative Commons License

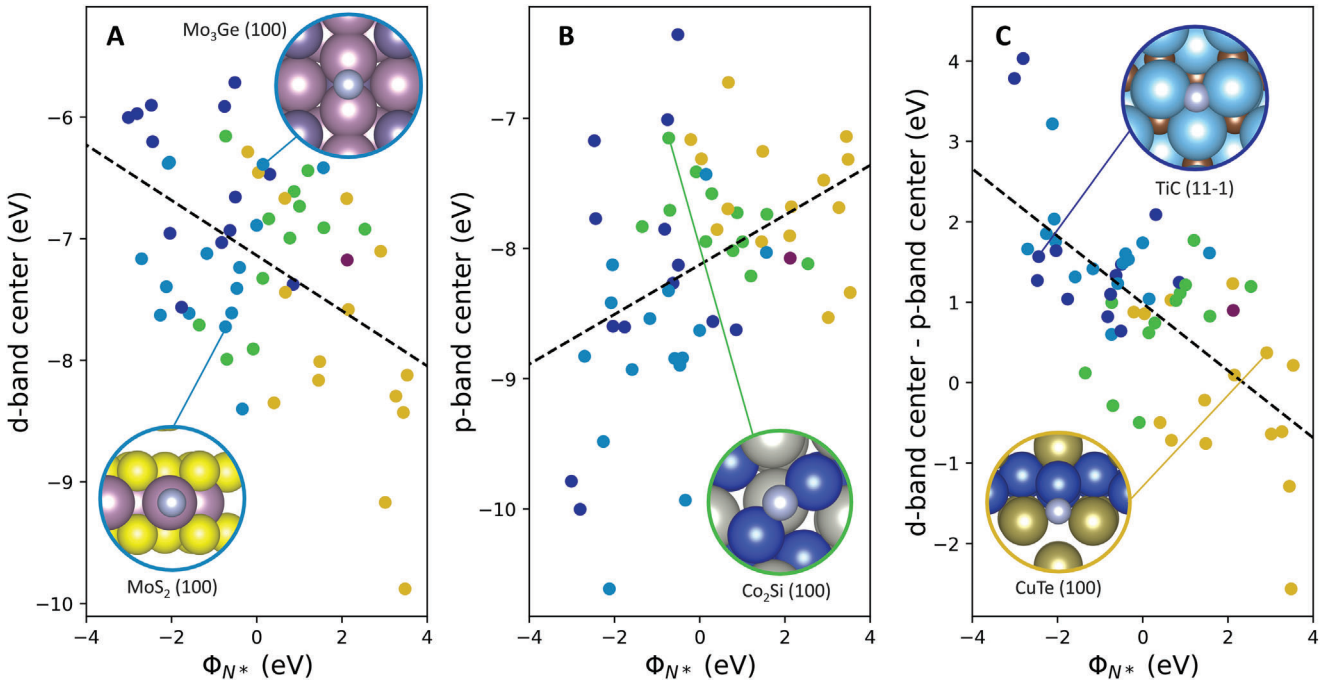

Figure 5. N^* binding energy scaling with surface atom band centers. A) *d*-band center, B) *p*-band center, and C) difference between *d*-band and *p*-band centers projected onto atoms within the coordination environment of the N^* adsorbate. *d*-bands are projected onto metal atoms and *p*-bands onto covalent atoms. r^2 values are 0.22, 0.16, and 0.42 for A, B, and C, respectively. Select surface structures with adsorbed N^* are shown to illustrate the geometric complexity of the BCAs. MoS_2 (100) coordinates N^* to one metal atom while Mo_3Ge (100) and TiC (11$\bar{1}$) both coordinate N to more than two metal atoms. Co_2Si (100) and CuTe (100) are both examples of surfaces that favorably coordinate to non-metal active sites.

energies on flat and stepped monometallic surfaces (Figure S5, Supporting Information) because the *s* and *p* bands share a broadly delocalized free-electron-like state,[34] while the *d*-band dominates the local electronic character.[35] This leads to a nearly ideal *d*-band theory type of adsorption in which the electrostatic interaction of the surface with the adsorbate remains nearly constant between surfaces, while the formation of surface-adsorbate bonding and anti-bonding states, which depend on the localized electronic character, changes considerably between surfaces.[36] However, for covalently doped surfaces, previous studies indicate that binding energies are less strongly correlated to *d*-band centers, especially when adsorbing at non-metal active sites, and the *p*-band center may be a relevant descriptor of surface reactivity.[37–39]

To probe these electronic effects for BCA materials, both the surface *d*-band and *p*-band centers were plotted against N^* binding energies for a subset of the BCAs. As shown in **Figure 5**A,B, there is almost no systematic scaling of the surface atom band centers with N^* binding energy across the set of BCAs. This result contrasts starkly with the *d*-band behavior of NRR on simple metals (Figure S5, Supporting Information), which scale strongly with N^* adsorption energy with an r^2 value of 0.87. For the BCA materials, we find a stronger correlation between N^* binding and the difference in the *d*-band and *p*-band center energies (Figure 5C), which has previously been used to rationalize doping effects in small sets of *p*-doped alloys.[40,41] However, this electronic descriptor has not previously been applied to a large set of binary/multinary materials to explain activity trends.

For the BCAs considered here, a larger, more positive *d*-*p* band difference (Δdp) arises from a higher lying *d*-band center and lower lying *p*-band center, whereas a lower Δdp is associated with a lower *d*-band center and higher *p*-band center. A larger Δdp indicates stronger N^* binding, which reduces as Δdp decreases. A larger Δdp arises from 1) a higher initial *d*-band center for the corresponding metal, and 2) reduced hybridization of the metal with the nonmetal, resulting from lower electronegativity and/or stoichiometry of the nonmetal. As hybridization of the metal *d*-states with the nonmetal *p*-states increases, the *d*-band center descends and the *p*-band center rises to yield more overlapping states, thereby reducing Δdp. This increased hybridization and consequent oxidation of the metal by the nonmetal yields a metal active site that is less reactive and less capable of reducing adsorbates (i.e., weaker N^* binding, Φ_{N^*}). Moreover, a higher *p*-band center reduces adsorbate binding to the covalent species.[39] Other research has also identified trends in reactivity of the active site with its oxidation state brought on by hybridization with bulk covalent species.[42] These electronic effects provide a justification for the BCA trends in the NRR volcano: the more reactive BCAs tend to be comprised of more reactive TMs paired with less electronegative nonmetals, and this reactivity is reduced (lower Δdp) in systems with less reactive metals and/or greater oxidation of the metal by the nonmetal, generally occurring via increased electronegativity and/or stoichiometry of the nonmetal. This also explains why some BCAs with early- to mid-d block TMs lie on the less reactive, right side of the volcano, whereas no late-TM based BCAs occur on the reactive left side of the volcano (i.e., no promotion of more noble metals by the nonmetal).

© 2024 Wiley-VCH GmbH

16146840, 0, Downloaded from https://onlinelibrary.wiley.com/doi/10.1002/aenm.202304559 by Office Of Scientific And Technical Information, Wiley Online Library on [28/05/2024]. See the Terms and Conditions (https://onlinelibrary.wiley.com/terms-and-conditions) on Wiley Online Library for rules of use; OA articles are governed by the applicable Creative Commons License

Despite its improved correlation with N^* binding and underlying chemical justification, we do not expect Δdp to independently serve as a quantitative descriptor for NRR activity, due to its relatively low correlation with Φ_{N^*} (r^2 of only 0.42). This poor correlation may arise in part from the non-uniform localization of electron density at the adsorption site, which results from hybridization with covalent dopants. However, Figure 5 highlights the additional layer of complexity that we propose is responsible for the challenges of accurately correlating N^* binding with electronic descriptors: the surface facets have highly variable compositions and surface geometries, with variable N^* coordination number (Figure S10, Supporting Information), different active site topologies (i.e., *z*-axis variability), coordination to nonmetals, and variable distances between active site atoms and their corresponding coordination to other surface atoms. Thus, we hypothesize that accurate descriptors of N^* binding or NRR activity on materials in the higher levels of complexity (e.g., BCAs) must include features that represent the geometry of the active site coordination environment (i.e., material and facet specific), alongside electronic features. Several strategies exist to encode surface structure and predict chemical properties,[43,44] many of which have already seen success applied to molecular chemistry and some surfaces studies.[45–47] The generated dataset is available online (see experimental section) for machine learning follow-up studies.

4. Conclusion and Outlook

The results from the current study cover a broad set of BCAs with no consistent similarities between surface facet, active site geometry, cation or anion group number, bulk geometry, electronic structure, or cation/anion stoichiometry. Consequently, these results further exemplify the materials challenge of NRR, as the studied BCA space is predominantly limited by the scaling relations of monometallic metal surfaces. For materials that obey these scaling relations, HER activity will outcompete NRR activity, resulting in poor selectivity toward electrochemical NH_3 synthesis. However, several of the BCAs do break scaling relations in a favorable way, having smaller Φ_{max} values than would be predicted at the corresponding N^* binding energy. Despite this, most of these scaling-relation-breaking BCAs exist on the right side of the scaling volcano (e.g., Fe_3C (101), Ni_2P (001), RhO_2 (100), FeP (011)), where HER activity is dominant. Breaking scaling in this region of the volcano is associated with selective stabilization of the early NRR intermediates (e.g., N_2^*, N_2H^*) relative to N^* binding; however, even surfaces that significantly break scaling on the right side of the volcano will likely still be limited by poor NRR selectivity. Significantly, several BCA materials, notably TiC, Zr_2Si, CrP, and ZrN, exhibit promising reactivity in the more reactive upper left region of the scaling volcano where NRR selectivity is maximized within the scaling volcano limits. Furthermore, TiC and ZrN are known to be highly stable, in contrast to the monometallic metals in this region. Across the set of BCAs only one studied surface, CrP (010), possesses a lower Φ_{max} for NRR than HER, which results from breaking the HER scaling relations to over-bind H^*. Our results indicate that several BCA materials warrant deeper investigation, both computationally and experimentally, to validate the results presented here and elucidate additional factors that contribute to their promising predicted performance. This analysis does not estimate surface stability, which is necessary to assess the promise of each candidate as a practical catalyst for NRR. Further studies of NRR catalysts based on the recommendations we provide in this work should include a surface Pourbaix analysis to ensure these surfaces are stable in relevant electrochemical conditions.[48]

Based on the volcano diagram, the optimal location for discovering materials with higher NRR selectivity appears to be the upper left quadrant of the volcano, where surfaces have greater N^* binding ($\Phi_{N^*} < 1.5$ eV), and HER activity is lower due to over-binding of H^*. This is the region of the volcano plot where the NRR and HER scaling lines are nearest, suggesting that the highest selectivity toward NRR occurs in this region. Moreover, materials in this region have stronger N_2^* binding via greater N_2 triple bond activation, which should increase coverage of NRR intermediates relative to H^*. For the BCA catalysts considered here, this region of the volcano is highly populated by materials containing early- to mid-group TMs, generally coordinated with less electronegative anions, where the active sites remain less oxidized and more reactive toward NRR intermediates.

Materials that break scaling in this upper left quadrant of the volcano provide the greatest opportunity for next-generation NRR electrocatalysis. These materials need to selectively under-bind NH_3^* relative to their N^* binding energy to move above the truncating line of the volcano, which is limited by the minimally bias sensitive NH_3^* desorption step. Multiple studied BCAs enable this behavior (e.g., VP (100), TiC ($11\bar{1}$), Ti_2O (111)) and move above the NH_3^* scaling line at −0.5 V, albeit not sufficiently to provide greater predicted activity toward NRR than HER. Breaking HER scaling to over-stabilize H^* in this upper left region of the volcano (as observed for CrP (010)) is also a viable strategy to increase NRR selectivity. Further destabilization of NH_3^* to shift farther above the NRR volcano peak may be accomplished via tuning of sharp surface electronic states to selectively decrease hybridization with the NH_3^* frontier orbitals. Because NH_3^* overwhelmingly prefers to bind to singly coordinated top sites, the dz^2 orbitals on active sites could be manipulated to limit bonding (as observed for TiC ($11\bar{1}$)), or geometric modification could be used to block top sites and leave the hollow and bridge sites open to other NRR intermediate species. Moving to higher levels of material complexity may enable electronic and geometric surface environments that can achieve this selective NH_3^* destabilization. Modulation of the reactive site environment via photochemistry, ligand chemistry, magnetic fields, or other external driving forces may also be tuned to remove or destabilize adsorbed NH_3.

However, as these surfaces and reaction environments increase in complexity and the design space expands rapidly, the value of predictive screening descriptors substantially increases. The current work provides a firm foundation for understanding the classes of materials that are most promising to further tune, why these materials exist at promising regions of the scaling volcano, and how material complexity may be further increased to overcome scaling limitations in the optimal regions of the volcano. However, there remains an opportunity to transfer these findings into quantitative screening descriptors that can predict N^* binding energy to identify the location of a material on the scaling volcano *x*-axis, as well as prediction of NH_3^* and H^* binding energies to determine if the material can break NH_3^* scaling and outcompete HER. In the BCA space, we have determined

© 2024 Wiley-VCH GmbH

16146840, 0, Downloaded from https://onlinelibrary.wiley.com/doi/10.1002/aenm.202304559 by Office Of Scientific And Technical Information, Wiley Online Library on [28/05/2024]. See the Terms and Conditions (https://onlinelibrary.wiley.com/terms-and-conditions) on Wiley Online Library for rules of use; OA articles are governed by the applicable Creative Commons License

that conventional electronic descriptors such as the *d*-band and *p*-band centers are not predictive of Φ_{N^*} due to the highly variable active site geometries exhibited by the BCA surfaces. Our investigation revealed a more robust correlation between Φ_{N^*} and the difference in *d*-band and *p*-band centers. This descriptor provides a promising starting point for further improvement, particularly through the incorporation of structure-sensitive local bonding features. Modern machine learning models may provide a solution to achieving accurate binding energy prediction from surface properties alone, however extracting interpretable descriptors is challenging. The dataset of BCA catalysts containing over 4000 surface-adsorbate calculations is published online (https://github.com/cote3804/NRR_data) with structures and surface properties to facilitate these machine learning efforts. In time, the combination of predictive screening tools coupled with deeper chemical understanding of the relationship between material complexity and electrocatalytic activity may uncover advanced NRR electrocatalysts that substantially overcome scaling near the volcano peak to yield high activity and selectivity toward NRR. The potential impact of sustainable ammonia production makes this a critical and worthwhile problem to solve.

5. Experimental Section

DFT Calculation Parameters: All GC-DFT calculations in this study were performed using JDFTx.[49] All calculations used the PBE functional[50] and the Grimme D3 dispersion correction[51] to correct for vdW interactions. Core electrons were treated using ultra-soft psuedopotentials of the GBRV[52] v1.5 library. Kohn–Sham wavefunctions were expanded using a planewave basis that was bounded by a 20 Hartree cutoff energy, and charge density evaluations were bounded by a 100 Hartree cutoff. The number of bands was set to the larger of (n_v/2 + 10) or (1.2*n_v/2), where n_v signifies the number of valence shell electrons required to achieve neutral charge. The Brillouin-zone was sampled using k-points from a Monkhorst-pack k-point mesh with a density of 1000 and folding integers set by Pymatgen.[53] Kohn–Sham wavefunctions were minimized to a convergence of 10^{-7} Hartrees/step. The width of the Fermi distribution for state occupations was set to 10^{-3} Hartrees.

Surface calculations were performed using the direct-approach Grand-Canonical minimization.[8] Implicit solvation was implemented for all surface calculations using the CANDLE[15] solvation model of water with 0.5 M F^- and Na^+. Lattice parameters for all systems were optimized in the bulk phase with the L-BFGS[54] optimization algorithm to an energy convergence of 10^{-6} Hartrees/Step along with dimensionless Wolfe minimization criteria of 10^{-4} and 0.9 for energy and gradient, respectively. Atomic positions within the unit cell were optimized with the FIRE[55] optimization algorithm as implemented in ASE[56] for bulk and surface unit cells to an energy convergence of 10^{-4} eV/step or a force convergence of 0.04 eV $Å^{-1}$. Atoms in the lowest 1.8 Å of the supercell model of surfaces were frozen to their bulk position during geometry optimizations.

Grand canonical energies of reference molecules were calculated using JDFTx with the same criteria used for surface calculations, with all periodic boundary conditions turned off. Reference energies needed to calculate the grand free energies of N_2 adsorption and NH_3 desorption use electronic contributions to the Helmholtz free energy calculated using $A_{el} + S_{vib/tr/rot} - \mu N$, where A_{el} is the electronic contribution computed using a canonical DFT calculation, N is the number of electrons of the molecule in its neutral state and μ is the Fermi level. Reference electronic energies for these molecules are computed using canonical DFT, as they exhibit low solubility, and thus are not present as solvated species in the bulk electrolyte of an actual electrochemical system.[57] Rotational, translational, and vibrational contributions to the Helmholtz free energy are included by their entropic contributions and it is assumed that rotational and translational entropy is quenched fully upon adsorption. Reference energies for protons are described using a CHE approach with $\Phi_H = \frac{1}{2} A_{H_2} - \mu_{0V}$. A chemical potential of 4.66 eV[58] was used as μ_{0V} to reference to the SHE. Distributions for pCOHP were calculated following standard equations.[31] Elements of the Kohn Sham band function – atomic orbital "transfer matrix" were calculated by JDFTx using self-orthogonalized Löwdin projections. Example evaluations are available at github.com/benrich37/ultraSoftCrawfish.

Workflow Methods: Each material was checked for its stability and solubility in water by conducting a literature search to determine whether previous reports had found that it was synthesizable and stable in aqueous electrolytes (see Table S3, Supporting Information). Experimental synthesis, catalysis, and characterization papers were considered. Materials that were identified by previous work to be stable in air and/or water, and insoluble in aqueous solvent were retained as viable candidates for further evaluation. Furthermore, materials that were studied by previous electrochemical studies were retained. Materials that were reported in the literature to be unstable or soluble in water were excluded from further evaluation in this work. When insufficient data was available for a material, it was retained to provide a more comprehensive set of investigated materials, although those materials could prove to be poor candidates due to their instability in aqueous solutions. Bulk materials that met these criteria were promoted to the surface cutting step.

To create a relevant catalyst surface model from a bulk composition, surfaces must be cut from the bulk phase and these surfaces must be stable. However, evaluating the stability of surfaces requires calculating surface energies. For stoichiometric surfaces, where the surface composition matches the bulk composition, surface energies are well-defined.[59] However, for nonstoichiometric surfaces, surface energies are more difficult to calculate.[59–61] As an alternative to calculating surface energies, a heuristic surface screening algorithm developed by Sun and Ceder was used.[19] This algorithm assumes that the most stable surface facets are those that are the most coordinated. This assumption is justified by the fact that surface atoms are stabilized by their coordinating neighbors and surfaces with higher coordination numbers have fewer high-energy broken bonds. Sun's algorithm returns a histogram of the surface facets with high coordination numbers. Surfaces with the highest coordination number were chosen from this set and this number was further reduced by requiring that each unit cell had minimum distances between periodic images of 4.5 Å and < 50 atoms. The two most stable surface facets that met these conditions were passed on to subsequent screening steps. Only bulk structures that produced at least one viable surface facet were optimized and passed on to further screening steps. Some bulk structures had fewer than two surface facets that could be modeled with ≤ 60 atoms and sufficient thickness, while other surfaces failed to converge. Consequently, NRR reactivity was modeled for only 101 of the 172 possible lowest energy surfaces of the 86 bulk structures.

Adsorbates from the reduced screening set (N_2^*, N_2H^*, N^*, NH^*, and NH_3^*) were placed onto converged surfaces manually. Due to the geometric complexity of the materials set, it was challenging to create an automated adsorbate placement algorithm that would place adsorbates at consistent active sites across the surfaces considered. Instead, adsorbates were manually placed at an on-top site and a more highly coordinated site (i.e., bridge or hollow sites). Adsorbate binding configuration sampling was not performed comprehensively in screening **Step 4**, meaning that it is possible some lower energy adsorption sites were not sampled for all surfaces. For materials that made it to screening **Step 6**, all active sites were sampled. Catalytic activity was evaluated using Φ_{max}, which is described in more detail in the Supporting Information. Materials that had small Φ_{max} values or deviated substantially from the scaling relations on flat metal surfaces were studied further in screening **Step 6** by fully sampling binding configurations and calculating binding energies for all NRR intermediates in the associative distal pathway. Co_2Si (100), CrP (010), HfP (110), MoS_2 (100), TiC (11$\bar{1}$), TiS_2 (100), Zr_2Si (112), and ZrC (100) were promoted to the final screening step.

© 2024 Wiley-VCH GmbH

16146840, 0, Downloaded from https://onlinelibrary.wiley.com/doi/10.1002/aenm.202304559 by Office Of Scientific And Technical Information, Wiley Online Library on [28/05/2024]. See the Terms and Conditions (https://onlinelibrary.wiley.com/terms-and-conditions) on Wiley Online Library for rules of use; OA articles are governed by the applicable Creative Commons License

Supporting Information

Supporting Information is available from the Wiley Online Library or from the author.

Acknowledgements

All authors gratefully acknowledge support from the U.S. Department of Energy, Office of Science, Basic Energy Sciences (DE-SC0022247) and the National Science Foundation, Division of Chemistry (CHE-2400339). This work utilized computational resources from the National Energy Research Scientific Computing Center (NERSC) on the Perlmutter supercomputer.

Conflict of Interest

The authors declare no conflict of interest.

Data Availability Statement

The data that support the findings of this study are openly available in GitHub at https://github.com/cote3804/NRR_data, reference number 123.

Keywords

electrocatalysis, grand-canonical DFT, nitrogen reduction, scaling relations

Received: December 31, 2023
Revised: April 20, 2024
Published online:

[1] D. Sandalow, R. Aines, Z. Fan, Friedmann, J., C. McCormick, A.-K. Merz, C. Scown, Low Carbon Ammonia Roadmap, **2022**.
[2] D. Barker, T. Brown, N. Cook, Green ammonia, Royal Society, https://royalsociety.org/topics-policy/projects/low-carbon-energy-programme/green-ammonia/ (accessed: September 2022).
[3] C. Smith, A. K. Hill, L. Torrente-Murciano, *Energy Environ. Sci.* **2020**, *13*, 331.
[4] C. L. Muhich, B. D. Ehrhart, I. Al-Shankiti, B. J. Ward, C. B. Musgrave, A. W. Weimer, *WIREs Energy Environ.* **2016**, *5*, 261.
[5] G. Hochman, A. S. Goldman, F. A. Felder, J. M. Mayer, A. J. M. Miller, P. L. Holland, L. A. Goldman, P. Manocha, Z. Song, S. Aleti, *ACS Sustainable Chem. Eng.* **2020**, *8*, 8938.
[6] A. J. Martín, J. Pérez-Ramírez, *Joule* **2019**, *3*, 2602.
[7] H. Huang, D. Periyanagounder, C. Chen, Z. Li, Q. Lei, Y. Han, K.-W. Huang, J.-H. He, *Adv. Sci.* **2023**, *10*, 2205808.
[8] R. Sundararaman, W. A. Goddard III, T. A. Arias, *J. Chem. Phys.* **2017**, *146*, 114104.
[9] C. R. Tezak, N. R. Singstock, A. W. Alherz, D. Vigil-Fowler, C. A. Sutton, R. Sundararaman, C. B. Musgrave, *ACS Catal.* **2023**, *13*, 12894.
[10] J. H. Montoya, C. Tsai, A. Vojvodic, J. K. Nørskov, *ChemSusChem* **2015**, *8*, 2180.
[11] E. Skúlason, T. Bligaard, S. Gudmundsdóttir, F. Studt, J. Rossmeisl, F. Abild-Pedersen, T. Vegge, H. Jónsson, J. K. Nørskov, *Phys. Chem. Chem. Phys.* **2012**, *14*, 1235.
[12] D. Chanda, R. Xing, T. Xu, Q. Liu, Y. Luo, S. Liu, R. A. Tufa, T. H. Dolla, T. Montini, X. Sun, *Chem. Commun.* **2021**, *57*, 7335.
[13] J. Pérez-Ramírez, N. López, *Nat. Catal.* **2019**, *2*, 971.
[14] A. Vojvodic, J. K. Nørskov, *Nat. Sci. Rev.* **2015**, *2*, 140.
[15] R. Sundararaman, W. A. Goddard, *J. Chem. Phys.* **2015**, *142*, 064107.
[16] S. Kozuch, S. Shaik, *Acc. Chem. Res.* **2011**, *44*, 101.
[17] K. S. Exner, I. Sohrabnejad-Eskan, H. Over, *ACS Catal.* **2018**, *8*, 1864.
[18] A. Jain, S. P. Ong, G. Hautier, W. Chen, W. D. Richards, S. Dacek, S. Cholia, D. Gunter, D. Skinner, G. Ceder, K. A. Persson, *APL Mater.* **2013**, *1*, 011002.
[19] W. Sun, G. Ceder, *Surf. Sci.* **2018**, *669*, 50.
[20] F. Studt, *Front. Catal.* **2021**, *1*, 658965.
[21] T. Bligaard, J. K. Nørskov, S. Dahl, J. Matthiesen, C. H. Christensen, J. Sehested, *J. Catal.* **2004**, *224*, 206.
[22] J. K. Nørskov, J. Rossmeisl, A. Logadottir, L. Lindqvist, J. R. Kitchin, T. Bligaard, H. Jónsson, *J. Phys. Chem. B* **2004**, *108*, 17886.
[23] V. A. Lavrenko, L. A. Glebov, A. P. Pomitkin, V. G. Chuprina, T. G. Protsenko, *Oxid. Met.* **1975**, *9*, 171.
[24] S. Saha, B. M. Rajbongshi, V. Ramani, A. Verma, *International Journal of Hydrogen Energy* **2021**, *46*, 12801.
[25] S. Das, D. Dubois, M. S. I. Sozal, Y. Emirov, B. Jafarizadeh, C. Wang, V. Drozd, A. Durygin, Z. Cheng, *J. Am. Ceram. Soc.* **2022**, *105*, 3925.
[26] M. Pourbaix, *Atlas of Electrochemical Equilibria in Aqueous Solutions*, 2nd ed., Pergamon, Oxford **1974**.
[27] T. M. Buscagan, D. C. Rees, *Joule* **2019**, *3*, 2662.
[28] N. R. Singstock, C. B. Musgrave, *J. Am. Chem. Soc.* **2022**, *144*, 12800.
[29] G. Henkelman, A. Arnaldsson, H. Jónsson, *Comput. Mater. Sci.* **2006**, *36*, 354.
[30] X.-F. Li, Q.-K. Li, J. Cheng, L. Liu, Q. Yan, Y. Wu, X.-H. Zhang, Z.-Y. Wang, Q. Qiu, Y. Luo, *J. Am. Chem. Soc.* **2016**, *138*, 8706.
[31] V. L. Deringer, A. L. Tchougréeff, R. Dronskowski, *J. Phys. Chem. A* **2011**, *115*, 5461.
[32] Z. Niu, S. Fan, X. Li, Z. Liu, J. Wang, J. Duan, M. O. Tadé, S. Liu, *ACS Appl. Mater. Interfaces* **2022**, *14*, 35477.
[33] J. Wang, L. Zhang, Y. Wang, Y. Niu, D. Fang, Q. Su, C. Wang, *Dalton Trans.* **2022**, *51*, 15111.
[34] N. D. Lang, W. Kohn, *Phys. Rev. B* **1971**, *3*, 1215.
[35] J. K. Norsko, *Rep. Prog. Phys.* **1990**, *53*, 1253.
[36] B. Hammer, J. K. Norskov, *Nature* **1995**, *376*, 238.
[37] B. Ren, G. Wen, R. Gao, D. Luo, Z. Zhang, W. Qiu, Q. Ma, X. Wang, Y. Cui, L. Ricardez-Sandoval, A. Yu, Z. Chen, *Nat. Commun.* **2022**, *13*, 2486.
[38] A. Maibam, S. Krishnamurty, M. A. Dar, *Mater. Adv.* **2022**, *3*, 592.
[39] J. C. Ortiz-Rodríguez, N. R. Singstock, J. T. Perryman, F. P. Hyler, S. J. Jones, A. M. Holder, C. B. Musgrave, J. M. Velázquez, *ACS Appl. Mater. Interfaces* **2020**, *12*, 35995.
[40] Y. Liu, T. Sakthivel, F. Hu, Y. Tian, D. Wu, E. H. Ang, H. Liu, S. Guo, S. Peng, Z. Dai, *Adv. Energy Mater.* **2023**, *13*, 2203797.
[41] H. Lee, O. Gwon, K. Choi, L. Zhang, J. Zhou, J. Park, J.-W. Yoo, J.-Q. Wang, J. H. Lee, G. Kim, *ACS Catal.* **2020**, *10*, 4664.
[42] Z. Xu, J. R. Kitchin, *Catal. Commun.* **2014**, *52*, 60.
[43] D. P. Kovács, C. V. D. Oord, J. Kucera, A. E. A. Allen, D. J. Cole, C. Ortner, G. Csányi, *J. Chem. Theory Comput.* **2021**, *17*, 7696.
[44] A. P. Bartók, M. C. Payne, R. Kondor, G. Csányi, *Phys. Rev. Lett.* **2010**, *104*, 136403.
[45] D. S. Wigh, J. M. Goodman, A. A. Lapkin, *WIREs Comput. Mol. Sci.* **2022**, *12*, e1603.
[46] R. Gómez-Bombarelli, J. N. Wei, D. Duvenaud, J. M. Hernández-Lobato, B. Sánchez-Lengeling, D. Sheberla, J. Aguilera-Iparraguirre, T. D. Hirzel, R. P. Adams, A. Aspuru-Guzik, *ACS Cent. Sci.* **2018**, *4*, 268.
[47] S. Takamoto, S. Izumi, J. Li, *Comput. Mater. Sci.* **2022**, *207*, 111280.
[48] G. Gao, A. P. O'Mullane, A. Du, *ACS Catal.* **2017**, *7*, 494.
[49] R. Sundararaman, K. Letchworth-Weaver, K. A. Schwarz, D. Gunceler, Y. Ozhabes, T. A. Arias, *SoftwareX* **2017**, *6*, 278.
[50] J. P. Perdew, K. Burke, M. Ernzerhof, *Phys. Rev. Lett.* **1996**, *77*, 3865.
[51] S. Grimme, J. Antony, S. Ehrlich, H. Krieg, *J. Chem. Phys.* **2010**, *132*, 154104.

© 2024 Wiley-VCH GmbH

16146840, 0, Downloaded from https://onlinelibrary.wiley.com/doi/10.1002/aenm.202304559 by Office Of Scientific And Technical Information, Wiley Online Library on [28/05/2024]. See the Terms and Conditions (https://onlinelibrary.wiley.com/terms-and-conditions) on Wiley Online Library for rules of use; OA articles are governed by the applicable Creative Commons License

[52] K. F. Garrity, J. W. Bennett, K. M. Rabe, D. Vanderbilt, *Comput. Mater. Sci.* **2014**, *81*, 446.
[53] S. P. Ong, W. D. Richards, A. Jain, G. Hautier, M. Kocher, S. Cholia, D. Gunter, V. L. Chevrier, K. A. Persson, G. Ceder, *Comput. Mater. Sci.* **2013**, *68*, 314.
[54] D. C. Liu, J. Nocedal, *Math. Program.* **1989**, *45*, 503.
[55] E. Bitzek, P. Koskinen, F. Gähler, M. Moseler, P. Gumbsch, *Phys. Rev. Lett.* **2006**, *97*, 170201.
[56] A. Hjorth Larsen, J. Jørgen Mortensen, J. Blomqvist, I. E. Castelli, R. Christensen, M. Dułak, J. Friis, M. N. Groves, B. Hammer, C. Hargus, E. D. Hermes, P. C. Jennings, P. Bjerre Jensen, J. Kermode, J. R. Kitchin, E. Leonhard Kolsbjerg, J. Kubal, K. Kaasbjerg, S. Lysgaard, J. Bergmann Maronsson, T. Maxson, T. Olsen, L. Pastewka, A. Peterson, C. Rostgaard, J. Schiøtz, O. Schütt, M. Strange, K. S. Thygesen, T. Vegge, et al., *J. Phys.: Condens. Matter* **2017**, *29*, 273002.
[57] J. M. Clary, D. Vigil-Fowler, *J. Phys. Chem. C* **2023**, *127*, 16405.
[58] D. Gunceler, K. Letchworth-Weaver, R. Sundararaman, K. A. Schwarz, T. A. Arias, *Modelling Simul. Mater. Sci. Eng.* **2013**, *21*, 074005.
[59] K. Reuter, M. Scheffler, *Phys. Rev. B* **2001**, *65*, 035406.
[60] F. Yalcin, M. Wolloch, *Comput. Mater. Sci.* **2024**, *234*, 112799.
[61] E. Heifets, R. I. Eglitis, E. A. Kotomin, J. Maier, G. Borstel, *Phys. Rev. B* **2001**, *64*, 235417.

© 2024 Wiley-VCH GmbH

16146840, 0, Downloaded from https://onlinelibrary.wiley.com/doi/10.1002/aenm.202304559 by Office Of Scientific And Technical Information, Wiley Online Library on [28/05/2024]. See the Terms and Conditions (https://onlinelibrary.wiley.com/terms-and-conditions) on Wiley Online Library for rules of use; OA articles are governed by the applicable Creative Commons License